Characterization of Inverse Diffusion Flames with Methane and Hydrogen

Francisco Maria Machado Rosa Neves Vaz
francisco.vaz@tecnico.ulisboa.pt

Instituto Superior Técnico, Universidade de Lisboa, Portugal

December 2019

Abstract

Greenhouse gas emissions and their climate impact are forcing the combustion industry to devise clean and more efficient solutions. Contrary to conventional flame configurations, Inverse Diffusion Flames (IDF) combine benefits of premixed and diffusion flames, exhibiting extended lean flammability range and low soot production. Hydrogen, in turn, when blended with hydrocarbon-based fuels, can significantly enhance combustion processes and reduce emissions due to its unique properties. In this thesis, an experimental study was conducted to assess the impact of H_2 enrichment on the flame structure and emissions of a methane IDF in a multi-slit rectangular burner, under fuel-lean conditions. Fuel blends containing 0%, 25% and 50% H_2 were tested, the global equivalence ratio was varied between 0.2 and 1.0 and flame power fixed at 236 W. A PIV (Particle Image Velocimetry) analysis was performed and measurements of the CO_2, CO, UHC and NO_x emissions were attained. Two distinct flame structures were identified (Type I and II). It was found that H_2 addition does not create new flame structures but affects the stability range of Type I and II. PIV analysis demonstrated that a significant fraction of the central air jet escapes combustion in flame structure II. Efficiency was found to be dependent on flame structure, with Type I exhibiting better performance overall. Hydrogen enrichment lowered carbon-related emissions for both flame structures and reduced NO_x for flame Type I whereas the opposite was found for flame Type II. Finally, hydrogen enabled to maintain flame structure Type I for leaner conditions.

Keywords: Inverse Diffusion Flame, Hydrogen, Emissions, NO_x, Particle Image Velocimetry

1. Introduction

The impact of greenhouse gases on global warming [1] and the fast pace at which energy demand is increasing [2] are imposing the energy industry to reinvent itself. Notably, energy systems are striving to be cleaner and more efficient. In this context, a new flame configuration has been captivating more attention - the Inverse Diffusion Flame (IDF). IDF is a flame in which a central fuel jet is surrounded by outer fuel jet(s). If the air jet velocity is high enough, the outer fuel jet(s) are entrained by the air jet, mixing with each other, to form a partially premixed flame. It consists in a combination of diffusion and premixed flames, with wider range of stability than the premixed flames and lower pollutant emissions plus higher efficiency than diffusion flames. First studies of IDF featured a co-annular burner, as the one depicted in Figure 1 (a). Mikofski et al. [3] studied the effect of the Reynolds number of the central air jet (Re_{air}) on IDF height and structure, pointing out a double flame structure with a partially premixed flame base, followed by a normal diffusion regime with higher levels of soot production. Recently, a burner configuration

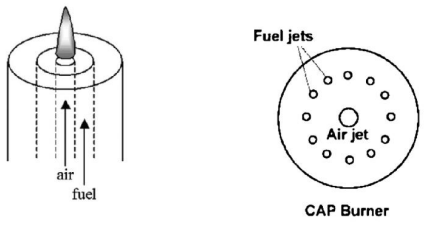

(a) CoA burner. Source: [3]. (b) CAP burner. Source:[4].

Figure 1: Co-anullar burner (CoA) and burner with circumferentially arranged fuel ports (CAP).

with Circumferentially Arranged fuel Ports (CAP), illustrated in Figure 1 (b), has been deserving more consideration. Sze et al., followed by others [4–7], reported improved flame stability and reactants mixing due to significant fuel entrainment by the central air jet. Dong et al. [6, 7] argued that flame structure is mainly dependent on Re_{air} and velocity

ratio between air and fuel ($V_r = V_{air}/V_{fuel}$), reporting a very wide range of Re_{air} and V_r with stable IDF. A dual structure flame was identified, with a flame base and a flame torch similar to a premixed flame, connected by a "neck like" structure with flow recirculation. This dual flame structure was also reported by Elbaz and Roberts with methane fuel [8]. Most of these studies were based on Liquefied Petroleum Gas (LPG) as a fuel [4–7, 9].

Regarding temperature and emissions of IDF, Dong et al. [6] reported maximum temperatures lower than 1800 K for lean conditions, with small dependency on Re_{air} for fixed V_r. NO_x emissions increased with decreasing V_r due to temperature increase while CO exhibited and opposite trend.

Recently, Ribeiro et al. [10] performed an extensive study in a multi-slit burner, such as the one represented in Figure 2. Ribeiro et al. used methane as

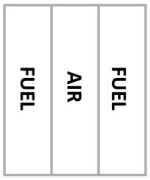

Figure 2: Schematic top view of the multi-slit rectangular burner.

fuel and focused on characterizing the IDF morphology. Chemiluminescence and Particle Image Velocimetry (PIV) analysis were performed. Three main flame structures were identified (lean, stoichiometric and rich). V_r showed great impact on flame structure, with higher velocity ratios resulting in enhanced mixing of air and fuel. A recirculation zone at the flame neck was found to be the main agent in stabilizing IDF with very low global equivalence ratios[1].

Hydrogen has great thermal and molecular diffusivity, high burning speed and low ignition energy [11–14]. When added to other fuels, it may increase flame temperature and enhance the heat release rate [15, 16]. Since it has no carbon, theoretically, its combustion leaves only water vapor behind, making it attractive as a possible substitute for carbon based fuels. A viable way of taking advantage of these hydrogen properties is to burn it along with a traditional hydrocarbon fuel [17].

Zhang et al. [18] proved that hydrogen improves stability of premixed methane-air flames. Kumar and Mishra [19] reported reduced laminar diffusion flame lengths with hydrogen addition to LPG fuel. Recent studies depict an increase in laminar burning velocity of premixed flames with H_2 addition [17, 20–22].

Concerning the impact of H_2 on emissions, studies point to soot reduction with H_2 addition to ethylene-air jet diffusion flames [23, 24]. CO emissions seem to reduce with H_2 addition [25]. Emissions of NO_x may reduce with H_2 addition, in spite of increased temperatures, according to Kumar et al. [19]. Han et al. [26] observed that methane-air H_2 enriched premixed flames exhibit lower NO_x emissions than diffusion flames in the same operating conditions.

Miao et al. [27–30], made experiments with LPG-H_2 fuel IDF in a CAP burner. These studies report a significant increase in the flame stability range with small H_2%. IDF with 50%H_2 and with 0%H_2 seem to have the same structural changes as the global equivalence ratio varies [27]. Further studies by Miao et al. [28] mention that LPG-H_2 IDF can hold stable with lower energy consumption than LPG IDF. Studies regarding emissions show that NO_x emissions may reduce with H_2 addition, for lean conditions. In general, very low global equivalence ratios are associated with high CO and UHC emissions. NO_x formation was associated with both Fenimore and Zeldovich mechanisms [30].

This work studies the impact of hydrogen addition to methane fuel in an IDF under fuel lean conditions and constant power, using a multi-slit rectangular burner. The only study found in literature related to hydrogen combustion through an IDF, until the date this thesis was written, features variable power and uses a CAP burner, which originates a completely different flame morphology compared to the multi-slit rectangular burner [6, 10]. Furthermore, there is also lack of information regarding flow velocity fields of IDF with hydrogen enriched fuels. The main goals of this work are to study the influence of the H_2 fuel proportion on flame morphology and emission characteristics. Namely, it is intended to understand if new flame morphologies are created through H_2 addition and if H_2 alters flame structure within the flame structures already present without it [10]. A velocity vector map of the flame flow is analyzed, to understand the mechanisms triggering flame structure changes through H_2 addition. Emissions of CO, CO_2, unburned hydrocarbons (UHC) and NO_x are extensively analyzed within a wide range of global equivalence ratios and three H_2 percentages. The emissions' results are cross-correlated with the flame structure's results so to investigate if the emission behavior of the flame is correlated with its morphology.

[1] Global equivalence ratio is dictated by the relative amounts of air and fuel supplied to the flame. Section 2 provides an important remark about the difference between global and local equivalence ratios throughout this text.

2. Experimental Analysis

This work is based on three main experiments: flame photography, flow velocity analysis and analysis of the flue gas released by the IDF. The experimental setup, for all of the experiments made, comprises a burning system, common for all experiments, and an acquisition system.

2.1. Burning System and Conditions

Figure 3 schematically represents the burning system. There are four flow meters for the fuel blend (Alicat Scientific, MC series). Two for methane (5 SLPM[2]) and two for hydrogen (1 SLPM). Hydrogen and methane are drawn from the research gas bottles (Alphagaz^{TM} model, with a purity higher than 99.95% (v/v)). Each flow splits in two and enters the flow meter. One of the hydrogen flows then mixes with one of the methane flows in a mixing chamber and the same happens for the other two flows. After mixing, each of the two fuel flows is then conducted into the lateral channels of the burner. Atmospheric air is fed to the flow meter by a compressing line, after passing through a filtering and drying process. It is then directly conducted to the central channel of the burner. The burner used is a two dimensional burner with three rectangular slits at the top (each slit: 38 mm x 2 mm), as illustrated in Figure 2. Based on most of IDF's studies

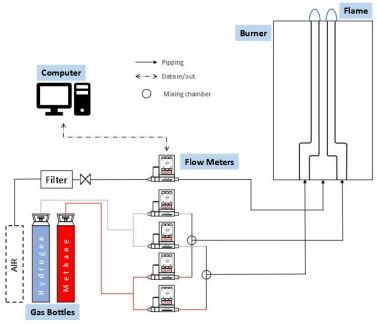

Figure 3: Scheme of the burning system.

in literature [4–7, 9, 27–31], a global equivalence ratio, dictated by the relative amounts of fuel and air supplied to the flame, will be used throughout this text (Equation 3). When the symbol "ϕ" or the term "equivalence ratio" are used, they concern to the global equivalence ratio. Conversely, if the local equivalence ratio is to be mentioned, the text will explicitly remark that the mentioned equivalence ratio is a local one, and not the global.

Volumetric percentage of H_2 on the fuel mixture was varied, keeping a constant power supplied to the flame - 236 W. The volumetric percentages of H_2 tested were 0%, 25% and 50%. The range of ϕ tested was $0.2 \leq \phi \leq 1.2$. The power supplied to the flame is given by:

$$P = \rho_{CH_4} \dot{Q}_{CH_4} \cdot LHV_{CH_4} + \rho_{H_2} \dot{Q}_{H_2} \cdot LHV_{H_2} \quad (1)$$

where ρ is the density, $\dot{Q}$ is the volumetric flow rate and LHV is the the lower heating value of the corespondent fuel component. For a certain power, the values of $\dot{Q}_{CH_4}$ and $\dot{Q}_{H_2}$ are found by defining the hydrogen's volumetric proportion on the fuel.

$$x_{H_2}(volume) = \frac{\dot{Q}_{H_2}}{\dot{Q}_{H_2} + \dot{Q}_{CH_4}} \quad (2)$$

For each x_{H_2}, Equation 2 is substituted on Equation 1 and the values of $\dot{Q}_{CH_4}$ and $\dot{Q}_{H_2}$ are obtained. Since, for each H_2% ($= x_{H_2} \times 100$), $\dot{Q}_{\text{fuel}}$ ($\dot{Q}_{\text{fuel}} = \dot{Q}_{CH_4} + \dot{Q}_{H_2}$) is constant, the equivalence ratio is varied by changing the volumetric flow rate of the central air jet, $\dot{Q}_{\text{air}}$. The equivalence ratio is calculated by:

$$\phi = \frac{\left(\frac{\dot{Q}_{air}}{\dot{Q}_{fuel}}\right)_{st}}{\left(\frac{\dot{Q}_{air}}{\dot{Q}_{fuel}}\right)} \quad (3)$$

where the subscript st stands for stoichiometric. As already mentioned, $\dot{Q}_{\text{fuel}}$ is obtained from the H_2% and flame power. The Reynolds number of the central air jet Re_{air}, is calculated by the following equation:

$$Re_{air} = \frac{\rho_{air} V_{air} D_h}{\mu_{air}} \quad (4)$$

where μ_{air} is the air viscosity, ρ_{air} is the air density and D_h is the hydraulic diameter of the cross section of the air jet flow, calculated based on [32]. Properties used to compute Equations 1 to 4 were evaluated at 0^{o}C, 1 bar.

2.2. Flame Photography

Figure 4 illustrates the experimental setup used for flame photography. The acquisition system involves a camera, lens and a computer. The burner was in a fixed position, aligned with the camera.

The camera used was a JAI CV-M9-GE, 3-CCD RGB with a resolution of 1074x768 pixels. The lens used were the Nikon AF NIKKOR 50mm f/1.4D lens. Images were acquired in RAW format, with null gain values. Lens aperture was set to its maximum, f/1.4, and minimum focus distance. Distance and alignment from the camera to the burner were kept constant for all burning conditions.

2.3. Particle Image Velocimetry

Particle Image Velocimetry (PIV) is a quantitative velocity measuring technique. This technique uses small tracer particles (alumina in this case)

[2]Standard litter per minute

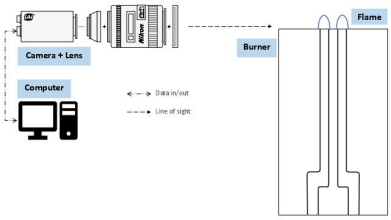

Figure 4: Scheme of the experimental setup for flame photography.

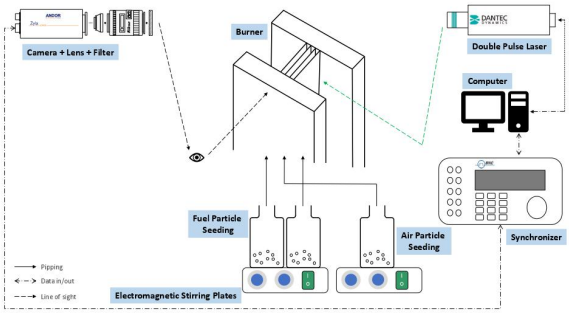

Figure 5: Scheme of the PIV experimental setup.

immersed in the flow under study. These particles that travel with the flow will then be illuminated by a double pulse laser in the area under study. The laser produces a planar sheet of green light, with a 532 nm wavelength. The laser is synchronized with a high speed camera, through a synchronizer connected to the central acquisition system. This camera will acquire two frames of the particles illuminated by the laser, such that each frame is taken at the exact moment in which the particles are illuminated by the laser pulse. Having two consecutive frames of the same illuminated particles and the time between the two laser pulses (Δt), allows for the determination of velocity. The final result is a 2D velocity field of the area under study.

Figure 5 schematically illustrates the experimental setup for the PIV analysis. The setup encompasses a camera, lens, filter, laser, synchronizer, computer, tracer particles, two magnetic stirring plates and rods and three bottles containing the particles. The particles (Logitech 5 micron Calcinated Aluminium Oxide Powder) are stirred through a magnetic rod which, in turn, is agitated by the electromagnetic stirrer (Roth MH 15 magnetic stirrer and Velp Scientifica ARE Aluminum). The flow of fuel/air passes through the correspondent bottle and drags the particles. This particles travel with the flow all the way up to the flame and are then lit by the laser and photographed by the camera. The camera used was the HiSense Zyla sCMOS, with a 40 fps frame rate and a resolution of 2560x2160 pixels. Attached to the camera was a Nikon AF NIKKOR 60 mm f/1.28D lens. A Meller Griot 532 nm optical filter was used. The laser utilized was a Dantec Dual Power 65-15 Yag, with two laser cavities, each with a maximum laser pulse frequency of 15 Hz and a wavelength of 532 nm. The synchronizer of these two devices was a BNC 575 Series Pulse Generator. Camera, laser and synchronizer were controlled by the software Dantec Dynamic Studio 5.1.

After the acquisition, a correlation between each pair of images acquired, to calculate the 2D velocity field has to be employed. Each image is divided into smaller rectangular interrogation areas (IA). The correspondent IA from each frame, are cross-correlated with each other to generate one velocity vector per IA. This correlation method is designated by cross correlation. Depending on the characteristics of each PIV experiment (type of flow, seeding system, etc), some variants of the cross correlation can be applied. In the case of this experiment, the average correlation was used. In the present study, only $\phi = 1$ and $\phi = 0.3$ were analyzed. $\phi = 1$ is associated to lower air velocities, so a $\Delta t = 200\mu s$ was used. Conversely, $\phi = 0.3$ is associated to higher air velocities, therefore, a $\Delta t = 60\mu s$ was required to achieve a reasonable resolution. The IA size used was constant: 16 px (horizontal) x 32 px (vertical). Vertical velocity components were much higher than horizontal, hence, vertical dimension of the IA is bigger than the horizontal. The overlapping factor, that overlaps adjacent IA so that particles near the border of the IA in the first frame aren't lost in the second frame [33]was set at 50% x 50%.

Table 1: Summary of PIV parameters.

Image pairs per acquisition	200
IA size (px)	16x32
Time between pulses	60 μs and 200 μs
Correlation	Average Correlation
Overlapping factor	50% x 50%

2.4. Flue Gas Analysis

Emissions from unburned hydrocarbons (UHC), CO, CO_2, and NO_x were analyzed. Figure 6 schematically illustrates the experimental setup of the acquisition system for the analysis of the flue gas species concentration. The system starts by collecting the flue gas sample with an L-shaped probe,

placed inside the hood's opening. The sampling gases are cooled as they travel within the probe. Afterwards, the sample passes through a condenser, a silica dryer and a cotton filter - moisture, particles and other condensates are removed. This circuit assures that a clean and dry sample will enter the gas analyzers so that they can properly present the concentration values in an Orsat (dry) reference basis. After the cotton filter, the sample passes through the pump and then through the flow meter, ensuring that the probe aspirates a constant flow of flue gas, that is adequate to enter the analyzers. Finally, the sample passes through the analyzers. The analyzers send an electric analogue signal to an acquisition board - Data Translator DT 9802 12 bit - which converts it to digital, at a sampling frequency of 100 Hz. The acquisition board is connected via USB to a computer, which runs the software HP VEE-LAB v5.02 to collect the data regarding the gas species concentration. The sampling period is 30 seconds for each measurement.

Flue gas measures directly read from the gas an-

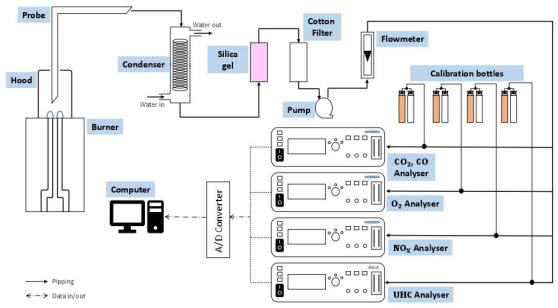

Figure 6: Scheme of the experimental setup for the flue gas analysis.

alyzers need to be further processed, in order to account for the dilution effect created by the exterior ambient air aspirated by probe. Since power supplied to the flame is constant, flue gas measures directly read from the gas analyzers were computed into kg (or g) of species emitted per MJ of burned fuel, as Turns suggests [34]:

$$\frac{Mass\,of\,species\,i}{Fuel\,energy\,supplied} = \frac{EI_i}{\Delta h_c} \tag{5}$$

where Δh_c is the heat of combustion of the fuel and EI_i is the emission index for species i, defined as the ratio of the mass of species i emitted to the mass of fuel burned by the combustion process [34]. Assuming that all of the carbon fuel appears in the combustion products in the form of CO, CO_2 and UHC, EI_i is given by [34]:

$$EI_i = \left(\frac{\chi_i}{\chi_{CO_2} + \chi_{CO} + \chi_{UHC}}\right)\left(\frac{xMW_i}{MW_f}\right) \tag{6}$$

where the χs are the volumetric fractions of the species analyzed (measured by the gas analyzers), x is the number of moles of carbon in a carbon fuel C_xH_y, and MW_i and MW_f are the molecular weights of the species i and the fuel, respectively. Using equation 5, emissions are reported in mass of species i emitted per amount of fuel energy supplied to the flame. Table 2 summarizes the fuel constants used to calculate the emission indices and the heat of combustion of the fuel.

Table 2: Summary of the fuel constants used to calculate the emissions.

$\%H_2$	x	y	MW_f (kg/kmol)	Δh_c (kJ/kg)
0	1	4	16	50000
25	0.75	3.5	12.5	52830.7
50	0.5	3	9	57800.6

3. Results

3.1. Flame Structure

Two distinct flame types were identified, Type I and Type II. Figures 8 (a) and (b) illustrate the visual appearance of flames Type I and II, respectively. The range of ϕ, for each $H_2\%$, in which each flame type holds stable is represented in Figure 7. Flame Type I has an "M" shaped body and fea-

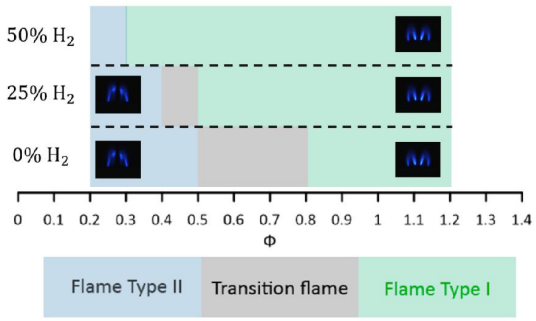

Figure 7: Equivalence ratio range for each type of flame, for each $H_2\%$.

tures two important flame regions, as indicated in Figure 8 (a). Flame Region A (FRA) is the main flame region, in which most of the fuel is entrained by the low pressure, high velocity central air jet. Its intense blue light shows that there is a good mixing of the reactants due to this entrainment effect [5, 9, 27, 31]. The second flame region, Flame Region B (FRB), corresponds to the burning of the fuel particles, that did not follow the air jet, with the adjacent ambient air [10] and features small luminosity. Flame length is roughly constant, for each $H_2\%$, in flame Type I.

As Re_{air} is increased, flame Type II will eventually be formed. It features a "neck-like" structure,

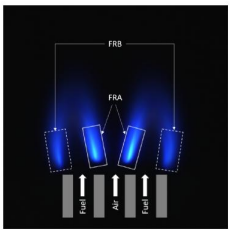

(a) Flame Type I - Flame regions ($\phi = 1$; $V_r = 19$; $0\%H_2$).

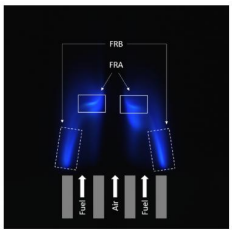

(b) Flame Type II - Flame regions ($\phi = 0.3$; $V_r = 63$; $0\%H_2$).

Figure 8: Flame types - description.

as reported by many other authors. [6, 7, 10, 27, 28]. The mass flow rate of air is so big that it creates a shear lifting force on FRA, shifting its position to a higher one, and making its luminosity and area become notably lower, as illustrated in Figure 8 (b). Miao et al. [28] reported three effects associated with escalating Re_{air}, which seem to apply in the present case: entrainment force on fuel due to negative pressure difference (1); shear lifting force acting on FRA (2); air jet momentum (3). Starting with Flame Type I and increasing Re_{air}, even if 1. promotes better mixing of the reactants and enhances combustion in FRA, effects 2. and 3. will prevail over 1. and flame structure will change to that of Flame Type II. High Re_{air} (and velocity) leads to a shear lifting force, pushing FRA upwards, stabilizing it downstream and reducing its area. The air jet is cold and has high momentum (high mass flow rate). FRA Type II is small and its reaction rate is not enough to preheat and ignite most of the air jet (and its entrained fuel).

In terms of flame structure, the effect of H_2 addition is divided in two possibilities: either it changes the flame type or it does not. Focusing on the case in which flame type does not change, consider, for example, Figure 9. Hydrogen, with small density and high thermal diffusivity, increases the reaction rate of the mixture [11, 35–38]. Therefore, even if flame structure is the same, stability is improved and flame length and width decrease. Furthermore, radiation within the visible region of the emission spectrum of the $0\%H_2$ flame tends to diminish with H_2 addition because hydrogen combustion emits ultraviolet radiation, not visible.

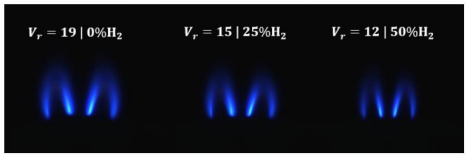

Figure 9: Evolution of flame Type I ($\phi = 1$) with H_2 addition on fuel.

Figure 10: Evolution of flame Type II ($\phi = 0.3$) with H_2 addition on fuel.

Going through the case in which flame structure changes, consider, for example, Figure 10. Due to its high heat of combustion and high thermal diffusivity, H_2 promotes a higher reaction rate and has lower ignition energy than CH_4 alone. Ignition of reactants is faster, temperature increases and so does reaction rate. The small FRA of flame Type II ignites the high momentum cold air jet and entrained fuel. FRA increases its area to form flame Type I and anchor the center of the flame.

3.2. PIV Analysis

Naturally, major changes of the flow velocity fields occur for the case in which flame structure is affected by hydrogen. Therefore, the main subject of this analysis is the discussion of the effects of hydrogen when it converts flame Type II into flame Type I.

3.3. Flame Type I vs Flame Type II

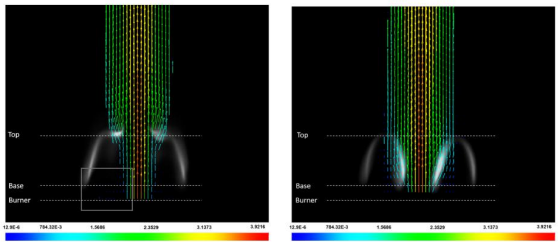

(a) Vector mapping - flame Type II ($\phi = 0.3$, $0\%H_2$, $\Delta t = 60ms$, $IA = 16x32$).

(b) Vector mapping - flame Type I ($\phi = 0.3$, $50\%H_2$, $\Delta t = 60ms$, $IA = 16x32$).

Figure 11: Vector mapping of flames Type I and II.

Figure 11 (a) shows the vector mapping of flame Type II ($\phi = 0.3$, $0\%H_2$). As Figure 11 (a) illustrates, first, by continuity and due to boundary layer effects, the air jet slightly expands after exiting the central slit. Immediately after the exit of the slits, the fuel jets are entrained by the low pressure central air jet. Subsequently, a narrow section arises, in which air and fuel improve their mixing quality due to high momentum diffusion from the central air jet to the fuel jets. Finally, that narrow section expands when it reaches FRA on the sides. It expands because FRA, being a combustion zone, is hot and releases the hot flue gases that expand and accelerate due to their decreased density [10, 39]. Recalling section 3.1.2, this flame is

highly inefficient - along that narrow section just mentioned, the entrained fuel mixes with the central air and, part of it, escapes combustion by passing in between the two FRAs.
Figure 11 (b) illustrates the vector mapping of flame Type I, with the same ϕ, but now with 50%H_2. By increasing the reaction rate, hydrogen will cause the flame to anchor in the burner and reduce its length. As soon as the air jet leaves the burner, it expands and mixes with the fuel entrained. Since now FRA Type I is present, combustion starts right after the exit of the burner and the combustion area is much higher. There is much more fuel being burned, by FRA Type I. Therefore, instead of having the narrow section that was seen in flame Type II, now there is FRA Type I in that zone. The reactants are very hot due to preheating and the flue gases are even hotter. By continuity, the hot, less dense gases will accelerate and expand. As it can been seen in the vector mapping, the flow field from flame Type I is much wider and adhered to the burner in contrast to the narrow and stretched flow field of flame Type II. The portion of air and entrained fuel that was escaping combustion is now being burned in FRA Type I and contributing to anchor the flow on the burner and to extend it laterally. Although this flame is actually much more efficient than Type II, it should be remarked that there is still a small fraction of the central air jet and, probably, some entrained fuel, that does not take part in the combustion process.

3.4. Flue Gas Analysis

Recalling that this work is focused on fuel lean conditions, the analysis in this section will, in general, start from stoichiometric conditions (higher ϕ) towards leaner conditions (lower ϕ). Since each discussion will be divided in flame Type I and flame Type II, it is important to recall Figure 7 and to consider the range of ϕ for the flame type under study, according to each H_2%.
The results for the emissions of UHC, CO and CO_2 are presented in Figures 12 (a), (b), and (c), respectively. UHC and CO have very similar evolutions since both of them are associated with incomplete combustion. In general, when ϕ decreases, the UHC and CO emissions increase. Conversely, CO_2 is associated with complete combustion, thus having an opposite trend - ϕ decreases, its emissions decrease too. Combustion is less efficient for leaner air-fuel mixtures. Miao et al. [30] also verified similar evolutions for UHC, CO and CO_2.

When Re_{air} increases, velocity of the air jet and entrained fuel also increases. Residence times are lower and there is less time for complete combustion. Combustion starts to be more incomplete and the emissions of CO and UHC slightly increase

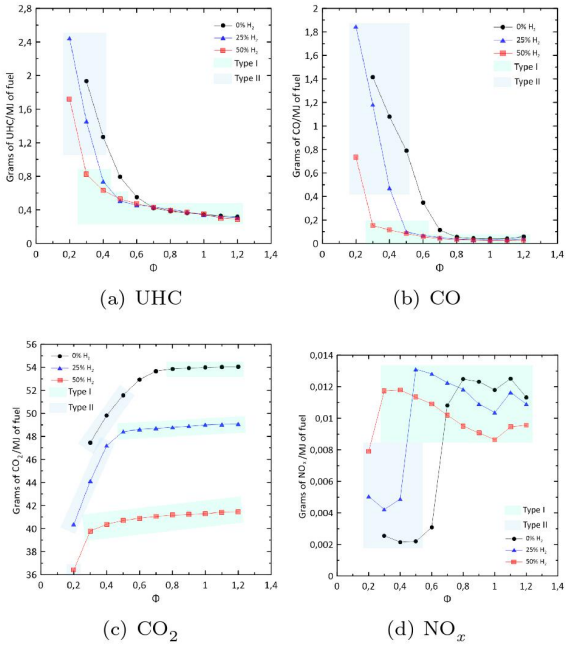

(a) UHC (b) CO

(c) CO_2 (d) NO_x

Figure 12: Variation of UHC, CO, CO_2 and NO_x emissions with ϕ for 0%, 25% and 50% of H_2. Highlighted sections of the plots correspond to emissions of flames Type I and II.

[4, 9, 30]. In contrast, but for the same reasons, CO_2 slightly decreases as Re_{air} increases.
To study the consequences of the fuel mixture's H_2% on flame Type I, consider, again Figures 12 (a), (b) and (c). The addition of H_2 reduces the carbon content of the fuel. Therefore, carbon related emissions, in general, are also reduced with H_2 addition. As Figure 12 (c) shows, there is a significant and expectable loss in CO_2 emissions as the H_2 content of the fuel increases. However, analyzing the emissions of UHC and CO from flame Type I, Figures 12 (a) and (b) do not show a significant decrease of those gases with H_2%. Consequently, H_2 does not seem to increase the efficiency of combustion. Miao et al. [30] also found that H_2% does not affect the emissions of CO and UHC for percentages lower than 60%.
Consider now the range of ϕ of flame Type II, according to each H_2%. As Re_{air} grows, there is an equivalence ratio, for each H_2%, triggering a steep increase of both UHC and CO, and a steep decrease of CO_2, which is the onset of the formation of flame Type II. Air jet velocity is higher, residence times are lower and combustion is incomplete. As for the case of flame Type I, for the case of flame Type II, increasing H_2% promotes a decrease of CO_2, UHC and CO emissions, due to reduction of the carbon content of the fuel.
Figure 12 (d) presents the variation of NO_x emis-

sions with the equivalence ratio for 0%, 25% and 50% of hydrogen on the fuel blend. Just like in the case of CO_2, UHC and CO, starting from $\phi = 1.2$, when ϕ decreases, there is a value of ϕ (for a specific H_2%) triggering a sharp decrease of the emissions and marking the transition from flame Type I to flame Type II. Consider, again, the range of ϕ of flame Type I, according to each H_2%. Starting from the lower equivalence ratios, there is a general decrease of NO_x emissions with ϕ until, $\phi = 1$. Previous studies [5, 6, 9] show that temperatures inside IDFs under fuel lean conditions are less than 1800 K, which cannot provide enough energy to activate the thermal-NO (Zeldovich) mechanism. In the previous section, it was reported that UHC emissions increase as Re_{air} also increases. The increase of UHC emissions, as stated before, is associated to incomplete combustion. Hence, its increase is associated to the rise of CH radicals in the flame, which can initiate the Fenimore mechanism [34]. Therefore, for flame Type I, NO_x emissions are higher for lower equivalence ratios, just like with UHC emissions in flame Type I. When ϕ increases from $\phi = 0.3$ (50%H_2), $\phi = 0.5$ (25%H_2) and $\phi = 0.8$ (0%H_2) to $\phi = 1$, NO_x emissions tend to decay since the same happens with UHC - when UHC emissions decrease, combustion tends to be more complete and the amount of CH radicals in the flame decreases, impeding the formation of NO_x by the Fenimore mechanism. Miao et al. [30] also reported a decrease of NO_x emissions from $\phi = 0.3$ to $\phi = 0.7$, and a further increase for richer conditions due to temperature rising which activates the Zeldovich mechanism and increases NO_x emissions. As Figure 12 (d) illustrates, in general, hydrogen addition tends to decrease the the amount of NO_x emitted for flame Type I. As stated before, for $\phi \leq 1$, NO_x emissions seem to be dominated by the Fenimore mechanism. As H_2 is added to flame Type I, the carbon content of the fuel reduces, reducing, in turn, the CH radicals produced. If CH radicals are reduced, the same happens to the NO_x emissions linked to the Fenimore mechanism. For $\phi \geq 1$, even though Zeldovich mechanism comes into play, Fenimore mechanism still has importance [34]. Therefore, the reduction of the carbon content of the fuel by the hydrogen addition will also reduce the NO_x emissions for $\phi \geq 1$.
Recall the range of ϕ of flame Type II, according to each H_2%. As transformation from flame Type I to Type II takes place, most of FRA Type I extinguishes, CH radicals stop being emitted and NO_x emissions from the Fenimore mechanism decay.

4. Conclusions

The two main goals of this work were to characterize the impact of fuel's hydrogen content on the flame structure and emission characteristics, under fuel lean conditions. To achieve this, a working range of stable flames was established. Global equivalence ratio varied from 0.2 to 1.2 and hydrogen content of the fuel was set at 0%, 25% and 50%H_2 by volume. For each H_2%, equivalence ratio and, hence, velocity ratio, was varied by varying Re_{air}. Power supplied to the flame kept at a constant value of 236 W. A summary of the most important findings of this thesis is presented below:

1. Based on its structure, two distinct flame types were identified, with two main flame regions: an inner flame region, FRA, where fuel burns with the central air jet and an outer flame region, FRB, where fuel burns with the exterior air. Flame Type I exhibits a luminous FRA, with considerable area and anchored to the top of the burner. Flame Type II is characterized by a smaller and less luminous FRA, stabilized in a higher position than FRA Type I.

2. Hydrogen addition to the fuel blend does not create new flame structures, in agreement with the results obtained by Miao et al. [27]. However, when H_2% is increased, the range of ϕ in which flame Type I holds stable is increased towards leaner conditions and the opposite trend is verified for flame Type II. With increasing H_2%, length, width and luminosity of flame Type I are reduced, whereas for flame Type II, structure changes to form flame Type I.

3. PIV analysis of both flame types reveals broader velocity profiles and flow fields of flame Type I than flame Type II. Furthermore, flame Type II features a significant portion of the air jet escaping combustion. The same phenomena is verified for flame Type I but on a much smaller scale.

4. Flame Type I reports very low or null emissions of CO and UHC and higher CO_2 emissions. Emissions of CO and UHC soar as flame Type II is formed and CO_2 emissions drop. These observations suggest that flame Type II is more inefficient than flame Type I.

5. Flame Type I presents a growing trend of NO_x emissions towards leaner conditions, possibly associated with the Fenimore mechanism. As flame Type II is formed and FRA Type I vanishes, NO_x emissions slump.

6. For both flame types, hydrogen addition reduces the carbon related emissions: CO_2 verifies considerable reductions and smaller reductions are reported for UHC and CO. Overall efficiency of the flame, apparently, is not much

affected by H_2 on the fuel blend. Emissions of NO_x for flame Type I decrease as H_2% is increased; the opposite trend is verified for flame Type II.

Acknowledgements
The author would like to thank Professor Mário Costa and Mr. Manuel Pratas for the provision of the gas analyzers from the Combustion Laboratory of IDMEC.

References

[1] NASA. Global climate change - vital signs of the planet. 2019.

[2] International Energy Agency IEA. World energy outlook - the gold standard of energy analysis. 2019.

[3] Mark A. Mikofski, Timothy C. Williams, Christopher R. Shaddix, A. Carlos Fernandez-Pello, and Linda G. Blevins. Structure of laminar sooting inverse diffusion flames. *Combustion and Flame*, 149(4):463–478, 2007.

[4] L. K. Sze, C. S. Cheung, and C. W. Leung. Appearance, temperature, and NOx emission of two inverse diffusion flames with different port design. *Combustion and Flame*, 144(1-2):237–248, 2006.

[5] L. K. Sze, C. S. Cheung, and C. W. Leung. Temperature distribution and heat transfer characteristics of an inverse diffusion flame with circumferentially arranged fuel ports. *International Journal of Heat and Mass Transfer*, 47(14-16):3119–3129, 2004.

[6] L. L. Dong, C. S. Cheung, and C. W. Leung. Heat transfer characteristics of an impinging inverse diffusion flame jet - Part I: Free flame structure. *International Journal of Heat and Mass Transfer*, 50(25-26):5108–5123, 2007.

[7] L.L. Dong, C.S. Cheung, and C.W. Leung. Heat transfer characteristics of an impinging inverse diffusion flame jet. part ii: Impinging flame structure and impingement heat transfer. *International Journal of Heat and Mass Transfer*, 50(25):5124 – 5138, 2007.

[8] A. M. Elbaz and W. L. Roberts. Flame structure of methane inverse diffusion flame. *Experimental Thermal and Fluid Science*, 56:23–32, 2014.

[9] L. L. Dong, C. S. Cheung, and C. W. Leung. Combustion optimization of a port-array inverse diffusion flame jet. *Energy*, 36(5):2834–2846, 2011.

[10] M.F. Ribeiro, F.M. Quintino, and E.C. Fernandes. Characterization of methane inverse diffusion flames in a multi-slot burner, 2019.

[11] Erjiang Hu, Zuohua Huang, Jiajia He, Chun Jin, and Jianjun Zheng. Experimental and numerical study on laminar burning characteristics of premixed methane–hydrogen–air flames. *International Journal of Hydrogen Energy*, 34(11):4876 – 4888, 2009. 2nd International Workshop on Hydrogen.

[12] Fabien Halter, Christian Chauveau, and Iskender Gökalp. Characterization of the effects of hydrogen addition in premixed methane/air flames. *International Journal of Hydrogen Energy*, 32(13):2585 – 2592, 2007. ICHS-2005.

[13] Ekenechukwu C. Okafor, Akihiro Hayakawa, Yukihide Nagano, and Toshiaki Kitagawa. Effects of hydrogen concentration on premixed laminar flames of hydrogen–methane–air. *International Journal of Hydrogen Energy*, 39(5):2409 – 2417, 2014.

[14] Ahsan R Choudhuri and S.R Gollahalli. Combustion characteristics of hydrogen–hydrocarbon hybrid fuels. *International Journal of Hydrogen Energy*, 25(5):451 – 462, 2000.

[15] Ahsan R. Choudhuri and S.R. Gollahalli. Characteristics of hydrogen–hydrocarbon composite fuel turbulent jet flames. *International Journal of Hydrogen Energy*, 28(4):445 – 454, 2003.

[16] S.A.A. El-Ghafour, A.H.E. El-dein, and A.A.R. Aref. Combustion characteristics of natural gas–hydrogen hybrid fuel turbulent diffusion flame. *International Journal of Hydrogen Energy*, 35(6):2556 – 2565, 2010.

[17] M. Reyes, F.V. Tinaut, B. Giménez, and José V. Pastor. Effect of hydrogen addition on the oh* and ch* chemiluminescence emissions of premixed combustion of methane-air mixtures. *International Journal of Hydrogen Energy*, 43(42):19778 – 19791, 2018.

[18] Yuyin Zhang, Jianghong Wu, and Satoru Ishizuka. Hydrogen addition effect on laminar burning velocity, flame temperature and flame stability of a planar and a curved ch4–h2–air premixed flame. *International Journal of Hydrogen Energy*, 34(1):519 – 527, 2009.

[19] P. Kumar and D.P. Mishra. Experimental investigation of laminar lpg–h2 jet diffusion flame. *International Journal of Hydrogen Energy*, 33(1):225 – 231, 2008. IWHE 2006.

[20] Erjiang Hu, Zuohua Huang, Jiajia He, and Haiyan Miao. Experimental and numerical study on lean premixed methane–hydrogen–air flames at elevated pressures and temperatures. *International Journal of Hydrogen Energy*, 34(16):6951 – 6960, 2009. 4th Dubrovnik Conference.

[21] Zhongqiu Li, Xiaobei Cheng, Wenming Wei, Liang Qiu, and Hui Wu. Effects of hydrogen addition on laminar flame speeds of methane, ethane and propane: Experimental and numerical analysis. *International Journal of Hydrogen Energy*, 42(38):24055 – 24066, 2017.

[22] Jie Liu, Xin Zhang, Tao Wang, Xiaosen Hou, Jibao Zhang, and Shizhuo Zheng. Numerical study of the chemical, thermal and diffusion effects of h2 and co addition on the laminar flame speeds of methane–air mixture. *International Journal of Hydrogen Energy*, 40(26):8475 – 8483, 2015.

[23] Ö.L. Gülder, D.R. Snelling, and R.A. Sawchuk. Influence of hydrogen addition to fuel on temperature field and soot formation in diffusion flames. *Symposium (International) on Combustion*, 26(2):2351 – 2358, 1996.

[24] Zhiwei Sun, Bassam Dally, Graham Nathan, and Zeyad Alwahabi. Effects of hydrogen and nitrogen on soot volume fraction, primary particle diameter and temperature in laminar ethylene/air diffusion flames. *Combustion and Flame*, 175:270 – 282, 2017. Special Issue in Honor of Norbert Peters.

[25] Hugo J. Burbano, Andrés A. Amell, and Jorge M. García. Effects of hydrogen addition to methane on the flame structure and co emissions in atmospheric burners. *International Journal of Hydrogen Energy*, 33(13):3410 – 3415, 2008. 2nd National and 1st Latin American Congress, Hydrogen and Sustainable Energy Sources.

[26] Han S. Kim, Vaibhav K. Arghode, Martin B. Linck, and Ashwani K. Gupta. Hydrogen addition effects in a confined swirl-stabilized methane-air flame. *International Journal of Hydrogen Energy*, 34(2):1054 – 1062, 2009.

[27] J Miao, C W Leung, C S Cheung, and R C K Leung. Flame Stability and Structure of Liquefied Petroleum Gas-Fired Inverse Diffusion Flame with Hydrogen Enrichment. 7(1):616–621, 2013.

[28] J. Miao, C. W. Leung, and C. S. Cheung. Effect of hydrogen percentage and air jet Reynolds number on fuel lean flame stability of LPG-fired inverse diffusion flame with hydrogen enrichment. *International Journal of Hydrogen Energy*, 39(1):602–609, 2014.

[29] J. Miao, C. W. Leung, C. S. Cheung, Zuohua Huang, and Wu Jin. Effect of H2 addition on OH distribution of LPG/Air circumferential inverse diffusion flame. *International Journal of Hydrogen Energy*, 41(22):9653–9663, 2016.

[30] J. Miao, C. W. Leung, C. S. Cheung, Z. H. Huang, and H. S. Zhen. Effect of hydrogen addition on overall pollutant emissions of inverse diffusion flame. *Energy*, 104:284–294, 2016.

[31] S. Mahesh and D. P. Mishra. Flame structure of LPG-air Inverse Diffusion Flame in a backstep burner. *Fuel*, 89(8):2145–2148, 2010.

[32] Frank P. Incropera, David P. Dewitt, Theodore L. Bergman, and Adrienne S. Lavine. *Fundamentals of Heat and Mass Transfer*. J. Wiley & Sons, 6 edition, 2007.

[33] Ken Kiger. PIV Basics: Correlation. In *SEDITRANS summer school on Measurement techniques for turbulent open-channel flows*, 2015.

[34] Stephen R. Turns. *An Introduction to Combustion Concepts and Applications*. McGraw-Hill, 3 edition, 2012.

[35] H. S. Zhen, Y. S. Choy, C. W. Leung, and C. S. Cheung. Effects of nozzle length on flame and emission behaviors of multi-fuel-jet inverse diffusion flame burner. *Applied Energy*, 88(9):2917–2924, 2011.

[36] D.P. Mishra and P. Kumar. Experimental investigation of laminar lpg–h2 jet diffusion flame with preheated reactants. *Fuel*, 87(13):3091 – 3095, 2008.

[37] F.H.V. Coppens, J. De Ruyck, and A.A. Konnov. The effects of composition on burning velocity and nitric oxide formation in laminar premixed flames of ch4 + h2 + o2 + n2. *Combustion and Flame*, 149(4):409 – 417, 2007.

[38] C.G. Fotache, T.G. Kreutz, and C.K. Law. Ignition of hydrogen-enriched methane by heated air. *Combustion and Flame*, 110(4):429 – 440, 1997.

[39] A. M. Elbaz and W. L. Roberts. Experimental characterization of methane inverse diffusion flame. *Combustion Science and Technology*, 186(9):1249–1272, 2014.